Atmos. Chem. Phys. Discuss., 13, 19051–19083, 2013
www.atmos-chem-phys-discuss.net/13/19051/2013/
doi:10.5194/acpd-13-19051-2013

Atmospheric Chemistry and Physics Discussions
Open Access

Biases in regional carbon budgets from covariation of surface fluxes and weather in transport model inversions

I. N. Williams[1], **W. J. Riley**[1], **M. S. Torn**[1], **S. C. Biraud**[1], **and M. L. Fischer**[2]

[1]Lawrence Berkeley National Laboratory, Earth Sciences Division, Berkeley, CA, USA
[2]Lawrence Berkeley National Laboratory, Environmental Energy Technologies Division, Berkeley, CA, USA

Received: 23 May 2013 – Accepted: 29 June 2013 – Published: 17 July 2013

Correspondence to: I. N. Williams (inw@uchicago.edu)

Published by Copernicus Publications on behalf of the European Geosciences Union.

Abstract

Recent advances in transport model inversions could significantly reduce uncertainties in land carbon uptake through assimilation of high frequency CO_2 concentration measurements. The impact of these measurements depends on the strength of covariation between surface fluxes and atmospheric transport and mixing at weekly and shorter time-scales, and on how well transport models represent this covariation. A stochastic boundary layer model was developed to quantify the effects of synoptic covariation on surface flux inversions at daily to season time-scales, and to compare covariation in transport model simulations to observations at the US Southern Great Plains Atmospheric Radiation Measurement Climate Research Facility. The most significant covariation of surface fluxes and transport occurred on weekly and longer time-scales, suggesting that surface flux inversions would benefit most from improved simulations of dynamics at the lower-frequency end of the synoptic spectrum. Biases in these rectifier effects contributed to surface flux biases of 13 % of the seasonal cycle amplitude, estimated from differences between observations and a data assimilation system (CarbonTracker). Biases in simulated covariation of transport and surface fluxes resulted in overestimated boundary layer concentrations during the growing season over the Southern Great Plains, by up to 0.3 ppm CO_2. Though small relative to the seasonal cycle, the strength of synoptic rectifier effects strongly varies on inter-annual time-scales, with some years having negligible and others having large vertical concentration gradients during the growing season, due only to differences in covariation of surface fluxes and transport. Inter-annual variability in vertical gradients due to synoptic rectifier effects is of similar magnitude to the inter-annual variability due to carbon sinks alone.

1 Introduction

Land and ocean ecosystems take up more than half of the carbon dioxide emitted by anthropogenic sources, but observational networks lack the coverage needed to

ACPD
13, 19051–19083, 2013

identify the regional ecosystem processes responsible for these sinks (Dolman et al., 2010). Current progress in transport model inversions could improve surface CO_2 flux estimates by assimilating concentration measurements in transport models at higher frequencies than previously possible (Liu et al., 2011; Gourdji et al., 2012). Transport model inversions are inferring surface fluxes from concentration variability measured at increasingly fine time-scales, from weekly down to daily and hourly, as continuous surface and airborne measurements become available (Masarie et al., 2011). Whether this higher frequency data assimilation arrives at more accurate estimates of regional carbon sinks will depend on how strongly surface CO_2 fluxes covary with atmospheric transport and mixing at these frequencies, and how well the underlying land surface and transport models simulate this covariation (Patra et al., 2008).

Solar radiation absorbed at the surface promotes both boundary layer turbulence and photosynthesis, driving diurnal and seasonal covariation of surface fluxes and boundary layer depth. Vegetation draws CO_2 from deeper boundary layers in summer and respires into shallower boundary layers in winter, enhancing boundary layer concentrations relative to the free-troposphere. These concentration gradients persist in annual averages even for annually balanced but seasonally varying ecosystem fluxes, analogously to an electrical rectifier that converts alternating to direct current (Denning et al., 1995). While deeper boundary layers dilute concentrations exchanged at the surface, transport by the divergent circulation determines how efficiently these concentrations are mixed with those of the overlying free-troposphere. These circulations become increasingly important in maintaining vertical concentration gradients at longer time-scales (Williams et al., 2011).

The time-scale dependence of concentration variability explains why concentration measurements often reflect an approximate balance between surface fluxes and boundary layer mixing at diurnal time-scales (Yi et al., 2004), and between surface fluxes and vertical transport at seasonal time-scales (Bakwin et al., 2004; Helliker et al., 2004; Lai et al., 2006). Yet neither of these approximations applies to concentration variability between diurnal and seasonal time-scales, referred to here as synoptic

ACPD
13, 19051–19083, 2013

variability. The synoptic covariation of boundary layer height and surface fluxes can create persistent concentration gradients similar to seasonal rectifier effects. Deeper boundary layers and stronger photosynthetic uptake coincide with enhanced insolation following the passage of synoptic weather systems, weakening the depletion of boundary layer concentrations relative to the free-troposphere in summer (Corbin and Denning, 2006). Alternatively, stronger vertical transport and mixing might accompany increased cloud cover and weaker photosynthetic uptake at some sites, which would magnify the depletion of boundary layer concentrations in summer.

Failure to adequately simulate synoptic rectifier effects could significantly bias inverse regional carbon sink estimates, which optimize surface flux estimates by minimizing differences between modeled and observed concentrations. Evidence for concentration biases include aircraft vertical profiling campaigns that found systematic biases in modeled vertical profiles of CO_2, where models that more closely matched the observed profiles inferred weaker northern and stronger tropical land carbon uptake (Stephens et al., 2007). Furthermore, clear sky biases in satellite observations will require transport models to assimilate concentration measurements with meteorology representative of the time and location of each remotely-sensed sample (Corbin and Denning, 2006; Parazoo et al., 2011). Surface flux biases could therefore result from assimilating satellite data in transport models that fail to adequately resolve the synoptic covariation of surface fluxes and atmospheric transport.

Previous studies inferred synoptic rectifier effects indirectly, from large variability in concentrations at synoptic scales during field campaigns (e.g. Lin et al., 2006), and from synoptic storm systems passing over CO_2 observing sites (Hurwitz et al., 2004). Full transport model simulations have demonstrated the effects of variability in boundary layer depth and transport on CO_2 concentrations (Chan et al., 2008), but have not isolated the effects of covariation. In this paper we develop a method to quantify the impact of synoptic covariation on surface flux inversions, by forcing a simplified transport model with surface and atmospheric data without covariation, or with covariation specified at each time-scale between daily and seasonal. We show that synoptic recti-

ACPD
13, 19051–19083, 2013

fier effects significantly impact surface flux inversions in some years, and are stronger in models than in observations over the Southern Great Plains (SGP), indicating the potential for further improvement in surface flux inversions through improved surface and boundary layer simulations, and higher-frequency data assimilation.

2 Stochastic boundary layer model for tracers (SBLM)

We developed a stochastic boundary layer model for tracers (SBLM), which consists of a tracer conservation equation for the boundary layer CO_2 concentration, and a stochastic model for surface fluxes and meteorological variables entering the conservation equation. The conservation equation is based on the well-mixed convective boundary layer approximation, and has appeared in similar forms as a diagnostic tool in previous studies of boundary layer CO_2 and other tracers (e.g. Betts, 1992; Styles et al., 2002; Williams et al., 2011). The boundary layer CO_2 mixing ratio is conserved according to

$$\rho_{\mathrm{m}} h \frac{\partial c_{\mathrm{m}}}{\partial t} + \rho_{\mathrm{f}} w_{\mathrm{e}} (c_{\mathrm{m}} - c_{\mathrm{f}}) + \rho_{\mathrm{m}} h \boldsymbol{v} \cdot \nabla c_{\mathrm{m}} = F_{\mathrm{sfc}} \tag{1}$$

where h, c_{f}, c_{m}, ρ, $\boldsymbol{v}$, and ∇ are the boundary layer depth, free troposphere and boundary layer CO_2 mixing ratios, atmospheric molar density, horizontal wind velocity vector, and horizontal gradient operator, respectively; subscripts (f and m) denote quantities at the free-troposphere level just above the boundary layer and averaged within the boundary layer, respectively.

The entrainment velocity (w_{e}) is given by

$$w_{\mathrm{e}} = \begin{cases} \frac{\mathrm{d}h}{\mathrm{d}t} - w + w_{\mathrm{cld}}, & \text{if } \frac{\mathrm{d}h}{\mathrm{d}t} - w + w_{\mathrm{cld}} > 0. \\ 0, & \text{otherwise.} \end{cases} \tag{2}$$

where w is the resolved-scale vertical wind velocity evaluated at the mixed layer height (positive upward), and w_{cld} is a sub-grid scale subsidence velocity due to convective

ACPD
13, 19051–19083, 2013

clouds (described further in Sect. 4.2). There is no entrainment into the boundary layer when the net movement of air is upward out of the boundary layer. The surface flux or net ecosystem exchange (F_{sfc}, in Eq. 1, positive upward) balances the local time rate-of-change of boundary layer CO_2 (first left-hand-side term), entrainment of free-troposphere CO_2 due to the combination of boundary layer growth into the free-troposphere and vertical advection by the subsiding flow (second term), and horizontal advection (third term).

Rearranging Eq. (1) to obtain a prognostic equation for the vertical concentration gradient,

$$\frac{\mathrm{d}}{\mathrm{d}t}\Delta c + E\Delta c = G(t) \tag{3}$$

where $\Delta c = c_m - c_f$ (hereafter referred to as the vertical gradient) is evaluated at a single point in the horizontal, and $G(t) = Fh^{-1}$. $F(t)$ is defined as

$$F = \left(F_{sfc} - \rho_m h \boldsymbol{v}\cdot\nabla c_m - \rho_m h\frac{\partial c_f}{\partial t}\right)\rho_m^{-1}$$

and the entrainment rate is defined as

$$E = \rho_f w_e/(\rho_m h)$$

The terms F, G, and E in Eq. (3) represent an external forcing similar to the forcing applied to single-column climate models for testing parameterization schemes. Those models are driven by time-series of temperature and water vapor horizontal advective tendencies, and mass divergence (divergence is analogous to the entrainment term E in Eq. 3).

We model F, E, and h as a linear system, which accounts for the covariance between these variables at each time-scale (τ), according to:

$$\boldsymbol{Y}(t) = \int_0^\infty \mathbf{q}(\tau)\boldsymbol{N}(t-\tau)\mathrm{d}\tau \tag{4}$$

ACPD
13, 19051–19083, 2013

where

$$\mathbf{q}(\tau) = \begin{pmatrix} q_{F,N_1} & q_{F,N_2} & q_{F,N_3} \\ q_{E,N_1} & q_{E,N_2} & q_{E,N_3} \\ q_{H,N_1} & q_{H,N_2} & q_{h,N_3} \end{pmatrix}$$

is a matrix of impulse response functions relating the input $\boldsymbol{N}(t)$ to the output $\boldsymbol{Y}(t)$. The input

$$\boldsymbol{N}(t) = \begin{pmatrix} N_1 \\ N_2 \\ N_3 \end{pmatrix}$$

is a vector of uncorrelated white-noise processes, randomly drawn from a Gaussian distribution with unitary variance, and the output

$$\boldsymbol{Y}(t) = \begin{pmatrix} F(t) \\ E(t) \\ h(t) \end{pmatrix}$$

is a vector containing the time-series we wish to model stochastically.

Since the impulse response matrix ($\mathbf{q}$) completely describes any linear system in general (Jenkins and Watts, 1969), the problem of modeling the time-series of F, E, and h reduces to finding the impulse response matrix that best approximates the system. The impulse response matrix is uniquely related to the cross-covariance matrix, given by

$$\mathbf{R}(\tau) = \int_{-\infty}^{\infty} \boldsymbol{Y}(t)\boldsymbol{Y}^{*}(t+\tau)\mathrm{d}t$$

with matrix conjugate transpose (*). The elements of $\mathbf{R}(\tau)$ are the cross-covariances of the variables in $\boldsymbol{Y}(t)$, which describe the covariances between each variable at each

ACPD
13, 19051–19083, 2013

time-scale (τ). It is easier to transform the problem from the time to frequency domains using the Fourier transform, where the impulse response matrix becomes the frequency response matrix (**Q**). The Fourier transform of the cross-covariance matrix, known as the cross-spectral density matrix, is given by

$$\mathbf{S}(f) = \begin{pmatrix} \mathrm{CSD}_{F,F} & \mathrm{CSD}_{F,E} & \mathrm{CSD}_{F,h} \\ \mathrm{CSD}_{E,F} & \mathrm{CSD}_{E,E} & \mathrm{CSD}_{E,h} \\ \mathrm{CSD}_{h,F} & \mathrm{CSD}_{h,E} & \mathrm{CSD}_{h,h} \end{pmatrix}$$

where f is the frequency (τ^{-1}). The elements of **S** are the cross spectral densities (abbreviated as CSD). Note that diagonal elements are the same as power spectral densities (PSD), and the matrix is Hermitian such that off-diagonal elements can be obtained from one another. Conceptually, the PSD distributes the variance as a function of frequency, whereas the CSD distributes the cross-covariance as a function of frequency.

The method of obtaining the impulse response matrix (**q**, or its Fourier transform, **Q**) from estimates of the cross spectral density (**S**) was derived by Ferraioli et al. (2010), and is outlined below (Eqs. 5–7). Multiplying Eq. (4) by $\boldsymbol{Y}(t+\tau')$ and taking Fourier transforms yields

$$\mathbf{S}(f) = \mathbf{Q}(f) \cdot \mathbf{I} \cdot \mathbf{Q}^*(f) \tag{5}$$

where **I** is the unit matrix corresponding to the cross-spectral matrix of the input white noise process (***N***). The eigen-decomposition of the cross-spectral matrix is

$$\mathbf{S}(f) = \mathbf{V}(f) \cdot \mathbf{\Sigma}(f) \cdot \mathbf{V}^{-1}(f) \tag{6}$$

where $\mathbf{V}(f)$ and $\mathbf{\Sigma}(f)$ are the eigenvector and eigenvalue matrices of $\mathbf{S}(f)$, respectively. Since **S** is Hermitian and its eigenvector matrix is unitary, i.e. $\mathbf{V}(f)\mathbf{V}^*(f) = \mathbf{I}$, Eqs. (5) and (6) can be combined to obtain the frequency response matrix

$$\mathbf{Q}(f) = \mathbf{V}(f) \cdot \sqrt{\mathbf{\Sigma}(f)} \tag{7}$$

ACPD
13, 19051–19083, 2013

where $\sqrt{\boldsymbol{\Sigma}(f)}$ is a diagonal matrix whose elements are the square roots of those in $\boldsymbol{\Sigma}(f)$.

The impulse response matrix acts as a filter on the input white-noise time-series ($\boldsymbol{N}$) to produce the stochastically-modeled time-series for F, E, and h, according to Eq. (4). The numerical method to solve Eqs. (4)–(7) (Ferraioli et al., 2010) requires only model cross-spectral densities, which can be estimated from transport model output or observations, as described in the following section.

3 Study site and methods

3.1 Input datasets

Measurements were made at the 60 m tower of the US Southern Great Plains Atmospheric Radiation Measurement Climate Research Facility (36.61° N, 97.49° W; hereafter referred to as SGP) between January 2002 and January 2010. More than 80 % of the Southern Great Plains is managed for agriculture and grazing, with winter wheat from November through June over 40 % of all land to the southeast, and pasture (40 %) and a mixture of C_3 and C_4 crops (20 %) from April through August (Cooley et al., 2005; Fischer et al., 2007; Riley et al., 2009).

Surface CO_2 fluxes were measured by eddy covariance at 60 m, using a 3-D sonic anemometer, and H_2O and CO_2 densities from an infrared gas analyzer. H_2O and CO_2 fluxes were calculated at 30 min intervals by block averaging scalar quantities, rotating coordinates to zero mean vertical and meridional wind speed, and correcting for effects of covariance between air density and turbulent vertical wind on fluxes (Webb et al., 1980). H_2O and CO_2 concentrations were obtained from a precision gas system (Bakwin et al., 1995) at 15 min intervals.

Observational time-series of boundary layer heights (h) were estimated from 4× daily balloon sonde profiles of potential temperature (Heffter, 1980). Observational estimates of vertical velocities were obtained from the North American Regional Reanalysis (Mesinger et al., 2006) at 32 km horizontal resolution and 25 hPa vertical resolution

ACPD
13, 19051–19083, 2013

every 3 h (NARR). Results using boundary layer heights from NARR were similar to sonde-derived estimates (not shown).

Measurement time-series at SGP were compared to the 2010 release of CarbonTracker, a carbon data assimilation system (Peters et al., 2007). CarbonTracker assimilates surface CO_2 concentrations with modeled transport and surface fluxes in a global, two-way nested atmospheric transport model (Transport Model 5, Krol et al., 2005; hereafter TM5) driven by meteorological fields from the European Centre for Medium-Range Weather Forecasts (ECMWF). The CarbonTracker data were averaged over the four horizontal grid points nearest to SGP, and include three-dimensional distributions of CO_2 concentrations and surface fluxes provided at $1^\circ \times 1^\circ$ spatial resolution every 3 h. We hereafter refer to the CarbonTracker surface fluxes and ECMWF meteorological forcing collectively as the CT-TM5 dataset.

The CT-TM5 dataset did not archive vertical advection, which we recreated using vertical velocities from the ECMWF interim reanalysis (Dee et al., 2011), based on the same general circulation model and parameterization schemes in TM5. Differences between CT-TM5 and our recreated advective tendencies could arise due to interpolation of the ECMWF meteorological data to 1×1 resolution in the CT-TM5 system, however averaging CarbonTracker and ECMWF output over different numbers of grid cells centered over the study site did not significantly influence our results. We used CT-TM5 concentrations averaged over the first two model levels above the boundary layer to define free-troposphere concentrations.

Prior surface fluxes serve as surface CO_2 boundary conditions in TM5. These priors are provided by CASA, a biogeochemical model (Potter et al., 1993), which is driven by ECMWF meteorological fields, including temperature, precipitation, solar radiation, and vegetation specified by satellite NDVI (Randerson et al., 1997). TM5 integrates concentration fields forward in time with the surface boundary conditions specified above, using three-dimensional winds from ECMWF to drive the transport. The effects of surface energy forcing on atmospheric boundary layer mixing are taken into account through the boundary layer diffusion scheme in TM5, which in turn depends on surface latent

ACPD
13, 19051–19083, 2013

and sensible heat fluxes predicted by the land surface scheme underlying the ECMWF reanalysis dataset (Viterbo and Beljaars, 1995). Transport and mixing by deep convection in TM5 is parameterized similarly to ECMWF.

CarbonTracker uses a Kalman filter that scales prior CASA fluxes by a linear factor updated each week, which optimizes surface flux estimates with respect to available observations (Peters et al., 2007). These scaled fluxes represent the assimilated surface fluxes in the final data product, often referred to as inverse surface flux estimates. Observational data assimilated in CT-TM5 currently include flask samples collected at surface sites as part of North American sampling networks, and CO_2 time-series from measurement towers.

3.2 Model-data synthesis

Cross-spectra were estimated for both observed and CT-TM5 time-series using the Daniell spectral estimator, following standard methods (e.g. von Storch and Zwiers, 2004). Seasonality and trends were accounted for by separating the time-series into spring (March–May), summer (June–August), autumn (September–November), and winter (December–February) seasons, and subtracting a quadratic polynomial fitted to each season for each year. The spectra were tapered in the time-domain using a cosine-bell weighting function. Our results were not sensitive to the choice of weighting function or the extent of smoothing using the Daniell window. Seasonal averages were taken over all years after estimating power and cross-spectra for each season of each year separately.

Using the cross-spectral densities as input to the stochastic model described in Sect. 2, we generated two sets of stochastically modeled time-series for F, E, and h, one each for the CT-TM5 and observational datasets. We refer to these time-series as the synthetic CT-TM5 and synthetic observations, and refer to the original time-series as the original CT-TM5 and original observed time-series. Note that the output time-series of the stochastic model are Gaussian-distributed, due to the linearity assumption underlying Eq. (4). To account for possible effects of skewness or extreme values, we

ACPD
13, 19051–19083, 2013

transformed the Gaussian distributions of the model output to match the original (univariate) distributions of F, E, and h, using the inverse transform sampling method (see Supplement). Examples of the modeled and original time-series are shown in Figs. S1, S2.

Equation (3) was integrated using finite differences by prescribing F, E, and h from the above linear system, to obtain Δc. While the original time-series are limited to the study period (8 yr), the synthetic time-series can have arbitrary length (here spanning 300 yr). These long time-series are useful in assessing statistically significant effects of weak to moderate covariation of F, E, and h on vertical concentration gradients.

4 Results

4.1 Power and cross spectra of synthetic time-series

Boundary layer height (h), entrainment (E), and CO_2 fluxes (F) have enhanced power at lower frequencies, without pronounced spectral peaks (Fig. 1). There are broad peaks at about the 4 day time-scale (frequencies between 0.2 and 0.3 cycles per day), particularly in power spectra of combined surface and horizontal CO_2 fluxes (F) (red lines in Fig. 1), most notably during the autumn and winter months. Processes that can contribute to power in surface and horizontal CO_2 fluxes at these frequencies include synoptic weather variability such as changes in radiation, temperature, and humidity accompanying transient storm systems, in addition to horizontal transport of CO_2. Lack of sharp synoptic spectral peaks is not surprising, as weather systems typically evolve from smaller to larger spatial scales over their life cycles, generating atmospheric variability over a broad range of time-scales (e.g. Vallis et al., 2004).

The power (top row of Fig. 1) and coherence spectra (middle row of Fig. 1) of the synthetic time-series closely match those of the original CT-TM5 time-series (cf. dashed and solid lines). Each time-series was normalized to have unit standard deviation (keeping the area under each PSD curve the same, preserving the shape of

ACPD
13, 19051–19083, 2013

the curves), to compare spectra across all three variables. Spectra of the observed time-series (Fig. 2, top row) have less power at low frequencies (i.e. shallower spectral slopes) than the CT-TM5 time-series (Fig. 1, top row), particularly for surface and horizontal CO_2 fluxes (F) and boundary layer height (h), during June–August, as discussed further in the following sections.

Cross spectra have both real (re) and imaginary (im) parts, shown as coherence and phase plots in the middle rows of Figs. 1 and 2. The (squared) coherence between two variables x and y is given by

$$\mathrm{Coh}_{x,y}(f) = \frac{|\mathrm{CSD}_{x,y}(f)|^2}{\mathrm{PSD}_x(f)\mathrm{PSD}_y(f)}$$

which is analogous to the squared correlation coefficient, if correlation were distributed as a function of frequency. We refer to squared coherence simply as coherence. The phase relation between the two variables x and y

$$\mathrm{Phase}_{x,y}(f) = \arctan\left[\frac{\mathrm{re}(\mathrm{CSD}_{x,y}(f))}{\mathrm{im}(\mathrm{CSD}_{x,y}(f))}\right]$$

quantifies how much the crests of time-series y lag the crests of time-series x at each frequency, in terms of a phase angle. A phase angle of 0.5 cycles at a frequency of 0.1 cycles per day (period 10 days) indicates crests of x are aligned with troughs of y and that crests in y follow troughs in x after 5 days, for example. Note that phase angles of -0.5 and $+0.5$ cannot generally be distinguished.

The CT-TM5 time-series are only weakly coherent at most frequencies (middle row of Fig. 1), with the exception of coherence between entrainment (E) and boundary layer height (h), which turns out to have a relatively small impact on vertical concentration gradients (shown in the following section). Both $\mathrm{Coh}_{F,h}$ (red lines in Fig. 1, middle row) and $\mathrm{Coh}_{F,E}$ (green lines in Fig. 1, middle row) have maxima at frequencies around 0.25×10^{-1} cycles per day (period of 4 days) in autumn and winter, consistent with

ACPD
13, 19051–19083, 2013

the synoptic time-scale. Coherence is weaker in observations compared to CT-TM5 (cf. middle rows of Figs. 1, 2), suggesting that the dynamical models underlying CT-TM5 are overestimating the coupling of atmospheric dynamics and surface fluxes at this site. Spectra shown in Figs. 1, 2 were estimated for time-series extending from January 2002 to Jaunary 2010 for CT-TM5 and January 2003 to January 2010 for observations. We found that coherence varies from year to year, which we explore in Sect. (4.3).

Phase angles (lower panels of Figs. 1, 2) are around 0.5 cycles at frequencies where coherence and power are greatest (e.g. 0.1 cycles per day), and are similar between both observed and CT-TM5 datasets. CO_2 flux into the boundary layer (F) is most positive when boundary layer height fluctuations are most negative, indicating that the shallowest daytime boundary layer heights coincide with reduced photosynthetic uptake (enhanced respiratory release). The strongest entrainment rates (most negative E) coincide with enhanced photosynthetic uptake and reduced respiratory release. These results are consistent with stronger solar heating at the surface driving both enhanced photosynthesis, deeper mixing, and stronger vertical transport.

4.2 Synoptic rectifier effect

Long simulations of the stochastic boundary layer model (SBLM) were designed to detect responses in vertical concentration gradients to covariance between the external forcing variables F, E, and h. We performed 300 statistically independent integrations of SBLM for each season, using synthetic time-series for F, E, and h as external forcing for each simulation (using Eq. 3). We tested the SBLM capability of predicting vertical concentration gradients by comparing power spectra of original CT-TM5 concentration gradients (i.e. those predicted by the CarbonTracker data assimilation system) to those predicted by SBLM forced with synthetic CT-TM5 time-series of F, E, and h. SBLM (blue dashed lines in Fig. 3) and CT-TM5 (red lines in Fig. 3) power spectra were consistent after accounting for uncertainty in the entrainment rates diagnosed using Eq. (2), as shown by the range of grey shading in Fig. 3. Concentration gradient power

ACPD
13, 19051–19083, 2013

spectra are shown in Fig. 3 in the form of log-log plots, due to their larger range of values.

Without sub-grid scale entrainment, entrainment of free-troposphere air into the boundary layer would occur only during resolved-scale subsidence, or when boundary layer growth exceeds the rate of resolved-scale ascent. In models however, resolved-scale ascent typically coincides with moist convection (Lawrence and Salzmann, 2008), which brings free-troposphere air into the boundary layer through parameterized mixing intended to represent the sub-grid scale compensating subsidence surrounding cumulus clouds, and the effects of rainy, evaporatively-cooled downdrafts. These parameterized mass fluxes are not archived in model or reanalysis data products and occur at smaller scales than represented by resolved vertical velocities in Eq. (2).

We accounted for the effects of boundary layer entrainment due to sub-grid scale cloud mass fluxes by modifying the entrainment rate with a parameter f, expressed as a fraction of the resolved-scale vertical velocity. This parameter is a function of time and takes on the values

$$f(t) = \begin{cases} f_o = \text{constant}, & \text{if } w(t) > 0. \\ 0, & \text{otherwise.} \end{cases}$$

We added this term to the entrainment velocity by defining the sub-grid scale entrainment term in Eq. (2) as

$$w_{cld} = -f \cdot w \tag{8}$$

under the assumption that sub-grid scale compensating subsidence scales (in magnitude) with the resolved-scale ascent (Lawrence and Salzmann, 2008). Our entrainment parameterization is similar in form to others (e.g. Stull, 1988, their Eq. 11.2.2.b), and reduces to the equilibrium boundary layer model in Bakwin et al. (2004) for $f_o = 1$ (i.e. upward convective mass fluxes are exactly compensated by subsidence).

We explored a range of solutions for entrainment parameters ranging from $f_o = 0$ (no compensating subsidence), to $f_o = 1.25$ (compensating subsidence 25 % greater than

ACPD
13, 19051–19083, 2013

the resolved-scale ascent), as shown by the gray shading in Fig. 3. SBLM correctly predicted the original CT-TM5 spectra for $f_o \approx 1$ (dashed blue lines of Fig. 3). The distribution of power shifts toward higher frequencies (i.e. shallower spectral slopes) as f_o increases (gray shading in top panels of Fig. 3), reflecting the tendency for resolved-scale ascent to occur over short time intervals associated with transient deep convection.

Seasonal concentration gradients in SBLM (dashed blue lines in Fig. 4) agree with the original CT-TM5 gradients (red line in Fig. 4) for the range of entrainment rates explored here. Boundary layer CO_2 becomes depleted in summer (June, July, and August), slightly enhanced in spring and autumn, and significantly enhanced in winter. The magnitude of the peak-to-trough seasonal cycle in vertical concentration gradients at SGP (3.4 ppm CO_2) is smaller than that at other continental sites across the Northern Hemisphere (4.4 ppm CO_2, Stephens et al., 2007).

We experimented with different forcing time-series to isolate the role of synoptic variability in generating vertical gradients. We quantified the effects of covariation of surface fluxes and boundary layer entrainment (as represented by $CSD_{F,E}$) by setting the other two cross-spectral densities ($CSD_{F,h}$ and $CSD_{E,h}$) to zero and generating synthetic forcing time-series having only covariation between surface fluxes and boundary layer entrainment (Fig. 5d, green lines). We similarly isolated the effects of $CSD_{F,h}$ (Fig. 5d, red lines), and $CSD_{E,h}$ (Fig. 5d, blue lines), for both the CT-TM5 (dashed lines) and observational time-series (solid lines). The total synoptic rectifier effect due to all three covariance terms is shown in Fig. (5a). Uncertainty in cloud mass fluxes did not significantly change our conclusions about the relative strengths of each rectifier effect, as shown by varying (f) between 0.75 and 1.25 (error bars in Fig. 5). Effects of distribution skewness (i.e. non-Gaussian distributions in forcing time-series) were also tested but found to have little impact (results not shown), meaning that synoptic rectifier effects were not dominated by rare extreme events in CO_2 fluxes or boundary layer depths.

ACPD
13, 19051–19083, 2013

Boundary layer concentrations were enhanced by covariation between surface fluxes and boundary layer height (0.2 ppm CO_2 in summer), and less so by covariation between entrainment and boundary layer height (0.1 ppm CO_2 in summer), shown in Fig. 5d (dashed red and blue lines, respectively). On the other hand, boundary layer concentrations were depleted by covariation between surface fluxes and entrainment (−0.1 ppm CO_2 in summer, dashed green lines in Fig. 5d). These opposing effects resulted in a net enhancement of about 0.13 ppm in boundary layer CO_2 in summer (Fig. 5a, JJA), or 9 % of the mean vertical gradient in summer at SGP, for the synthetic CT-TM5 forcing time-series. Synoptic rectifier effects in other seasons were generally smaller than in summer. Horizontal mixing and transport could suppress spatially-localized synoptic rectifier effects over heterogeneous land surfaces such as SGP, because the covariation of atmospheric dynamics and surface CO_2 fluxes can depend on vegetation type. Since F includes both surface fluxes and horizontal advection, we ran separate simulations with horizontal advection removed, and found stronger rectifier effects (0.4 ppm in summer, not shown), indicating that our results represent conservative estimates for homogeneous land surfaces where horizontal advection would likely play a smaller role. These results are consistent with the dissipation of localized, high-frequency perturbations by gravity waves in atmospheric transport models (e.g. Liu et al., 2011). We leave analysis of spatial variability to future work and focus here on the important impact of time-series non-stationarity due to inter-annual variability.

4.3 Inter-annual variability

Precipitation extremes can have a strong influence on ecosystem productivity and land-atmosphere coupling over the mostly non-irrigated Southern Great Plains. We repeated the above analyses for two separate years, 2006 and 2007, to quantify effects of non-stationarity resulting from unusually dry or wet summers. Synthetic forcing time-series were fitted separately to cross spectra for 2006, the second driest year in Oklahoma, and 2007, the wettest year on record for central Oklahoma (Dong et al., 2011). The results indicate much larger rectifier effects in summer 2007, with synoptic variability

ACPD
13, 19051–19083, 2013

generating vertical gradients of 0.3 ppm, or about 20 % of the average seasonal cycle amplitude in CT-TM5 (Fig. 5c, dashed lines), compared to negligible synoptic rectifier effects in summer 2006 (Fig. 5b, dashed lines). Covariation of surface fluxes and boundary layer heights explains most of the 0.3 ppm CO_2 synoptic rectifier effect during the wet year (Fig. 5f, dashed red lines). Synthetic observed forcing yielded qualitatively similar but much weaker rectified gradients compared to synthetic CT-TM5 forcing (cf. black and dashed lines in Fig. 5c). These results suggest stronger rectifier effects in CT-TM5 than observed due to stronger covariation between PBL depth and surface fluxes, indicating that land-atmosphere coupling may be too strong in the land surface and atmospheric models used in CT-TM5.

Cross-spectra explain why synoptic rectifier effects are stronger than average in 2007, during the summer months in CT-TM5 (Fig. 6). Coherence between surface fluxes and boundary layer depths is much larger in 2007 than over all years combined (cf. middle rows of Figs. 1 and 6, for June–August), particularly at lower frequencies corresponding to periods of about 10–20 days (thick lines in Fig. 6). The 2007 coherence spectra were separated into contributions from low (thick lines in Fig. 6) and high (dashed-dotted lines) frequencies with a separation frequency of 0.1 cycles per day (period of 10 days). We separated the effects of low frequency variability by weighting the cross spectra by a window that varies from 100 % for frequencies lower than 0.09 cycles per day (meaning that 100 % of the coherence in the original time-series is retained), to 1 % for frequencies above 0.11, with a smooth taper in between (split cosine bell). We repeated this procedure for high frequencies (retaining 100 % of coherence greater than 0.11 cycles per day). Phase angles of 0.5 cycles at these lower frequencies mean that high PBL depth coincides with negative surface CO_2 flux, or uptake (bottom panel of Fig. 6). Power spectra show enhanced variability in CO_2 flux at low frequencies, which also contributes to the larger rectifier effect in 2007 (cf. top panels of Figs. 1, 6), particularly for the spring and summer months.

We ran separate SBLM simulations with synthetic forcing time-series having coherence only at high or low frequencies, corresponding to the thick and dashed-dotted

ACPD
13, 19051–19083, 2013

lines in Fig. 6 (middle row). Integrating SBLM for the high and low frequency forcing separately shows that the 2007 summer synoptic rectifier effect in CT-TM5 resulted primarily from coherence between PBL depth and surface CO_2 fluxes at low frequencies having periods greater than 10 days (Fig. 7, solid line with downward-arrow markers). The higher frequencies account for one-third of the synoptic rectifier effect (Fig. 7, dashed-dotted line with upward-arrow markers). These results indicate potential for improvement in surface flux estimates through assimilation of concentration data at higher frequencies, considering that periodicities of 10 days require sampling time-scales of 5 days or shorter, and data assimilation systems currently update prior fluxes on weekly time-scales.

4.4 Impact on surface flux inversions

Biased synoptic rectifier effects could lead to biased surface CO_2 flux estimates in carbon cycle data assimilation systems, depending on how accurately the underlying prior flux models represent the true fluxes. We addressed this question by integrating SBLM in data-assimilation mode, using a simplified form of the Kalman filter used in transport model inversions, where we reduced the state vector to a scalar value for the summer surface flux at SGP. We used synthetic CT-TM5 entrainment rates and Eq. (3) as the transport model, with synthetic CarbonTracker surface CO_2 fluxes as a stand-in for a prior flux model. The solution to SBLM consistent with this synthetic forcing would represent a measurement time-series in the hypothetical case of perfect transport and prior fluxes, whereas here we subtract 0.2 ppm from this solution to simulate a +0.2 ppm bias in rectifier effects (in between the 0.1 ppm estimate for 2002–2010, and the 0.3 ppm estimate for 2007, from Fig. 5). Table 1 displays the results of the data assimilation tests for two different assumptions of prior flux uncertainty.

A +0.2 ppm bias in the synoptic rectifier effect leads to a $-0.15\,\mu mol\,m^{-2}\,s^{-1}$ surface flux bias when the model is constrained to closely match observed concentrations by specifying a large prior flux uncertainty of one standard deviation in F (denoted P_1 in Table 1). This negative flux bias allows SBLM to reduce boundary layer concentrations

ACPD
13, 19051–19083, 2013

relative to the free troposphere, to better match the synthetic measurement time-series. These biases represent 13 % of the peak-to-trough seasonal cycle amplitude at SGP. Though small relative to the seasonal cycle, the corresponding $-0.15\,\mu mol\,m^{-2}\,s^{-1}$ surface CO_2 flux biases compare in magnitude to inter-annual variability, as estimated from CT-TM5 standard deviations for summer surface CO_2 fluxes from 2003 to 2010 ($0.26\,\mu mol\,m^{-2}\,s^{-1}$). Reducing the prior flux uncertainties to 1 % of the standard deviation in F recovers the expected result that biases in concentration vertical gradients have no effect on surface flux estimates when constrained to match perfect prior fluxes (P_2 in Table 1). In that case, the 0.2 ppm CO_2 bias is left uncorrected in the assimilated data, and the surface flux is perfectly estimated. This example illustrates why it can be difficult to separate the effects of biases in transport from biases in prior fluxes when comparing modeled and observed concentration profiles.

5 Conclusions

Synoptic covariation of surface CO_2 fluxes and atmospheric transport can impact inverse surface flux estimates by generating vertical concentration gradients that persist on seasonal time-scales. Assimilating higher-frequency concentration measurements in transport models could therefore improve surface flux estimates, if the underlying transport and land surface models can accurately simulate this covariation. Two-thirds of the synoptic covariation of surface fluxes and transport occurs on time-scales longer than 10 days over the Southern Great Plains, suggesting that surface flux inversions would benefit most from improved simulations of dynamics at the lower-frequency end of the synoptic spectrum, for example through the representation of soil moisture and vegetation cover and their effects on surface fluxes and atmospheric transport. Biases in simulated rectifier effects can result in surface flux biases of 13 % of the seasonal cycle amplitude at SGP. Our results represent conservative estimates for homogeneous land surface types where horizontal advection would likely play a smaller role than at SGP.

ACPD
13, 19051–19083, 2013

Inter-annual variability can provide useful analogs of future-climate change for observationally testing carbon cycle models, such as comparing drought effects on simulated and observed carbon fluxes. Our results demonstrate that the strength of synoptic rectifier effects varies inter-annually, with a drought year (2006) having negligible synoptic rectifier effects, and a wet year (2007) having large synoptic rectifier effects during the growing season, due only to differences in covariation of surface fluxes and transport between years. This inter-annual variability in vertical gradients due to synoptic rectifier effects is of the same magnitude as that due to surface carbon sinks alone. Quantifying inter-annual variability in carbon sinks from concentration measurements will therefore require transport models that accurately resolve the covariation of surface fluxes and transport at synoptic time-scales.

This paper developed a new method to evaluate the reliability of carbon data assimilation systems, which provide critical links between carbon-cycle models and observations. Based on applications to the Southern Great Plains, we conclude that carbon data assimilation systems can be improved through better representation of synoptic-scale land-atmosphere covariation in underlying land surface and atmospheric transport models, and through assimilating concentration measurements at time-scales shorter than weekly. These improvements will help meet the challenges of testing carbon cycle models with limited observational data at ecosystem scales.

Supplementary material related to this article is available online at: http://www.atmos-chem-phys-discuss.net/13/19051/2013/acpd-13-19051-2013-supplement.pdf.

Acknowledgements. This work was supported by the Director, Office of Science, Office of Biological and Environmental Research, Climate and Environmental Science Division, of the US Department of Energy under Contract No. DE-AC02-05CH11231.

ACPD
13, 19051–19083, 2013

References

Bakwin, P. S., Tans, P. P., Zhao, C. L., Ussler, W., and Quesnell, E.: Measurements of carbon-dioxide on a very tall tower, Tellus B, 47, 535–549, 1995. 19059

Bakwin, P. S., Davis, K. J., Yi, C., Wofsy, S. C., Munger, J. W., Haszpra, L., and Barcza, Z.: Regional carbon dioxide fluxes from mixing ratio data, Tellus B, 56, 301–311, 2004. 19053, 19065

Betts, A. K.: FIFE Atmospheric boundary-layer budget methods, J. Geophys. Res.-Atmos., 97, 18523–18531, 1992. 19055

Chan, D., Ishizawa, M., Higuchi, K., Maksyutov, S., and Chen, J.: Seasonal CO_2 rectifier effect and large-scale extratropical atmospheric transport, J. Geophys. Res.-Atmos., 113, D17309, doi:10.1029/2007JD009443jd0094431.9, 2008. 19054

Corbin, K. D. and Denning, A. S.: Using continuous data to estimate clear-sky errors in inversions of satellite CO_2 measurements, Geophys. Res. Lett., 33, L12810, doi:10.1029/2006GL025910, 2006. 19054

Dee, D. P., Uppala, S. M., Simmons, A. J., Berrisford, P., Poli, P., Kobayashi, S., Andrae, U., Balmaseda, M. A., Balsamo, G., Bauer, P., Bechtold, P., Beljaars, A. C. M., van de Berg, L., Bidlot, J., Bormann, N., Delsol, C., Dragani, R., Fuentes, M., Geer, A. J., Haimberger, L., Healy, S. B., Hersbach, H., Holm, E. V., Isaksen, L., Kallberg, P., Koehler, M., Matricardi, M., McNally, A. P., Monge-Sanz, B. M., Morcrette, J. J., Park, B. K., Peubey, C., de Rosnay, P., Tavolato, C., Thepaut, J. N., and Vitart, F.: The ERA-Interim reanalysis: configuration and performance of the data assimilation system, Q. J. Roy. Meteor. Soc., 137, 553–597, 2011. 19060

Denning, A. S., Fung, I. Y., and Randall, D.: Latitudinal gradient of atmospheric CO_2 due to seasonal exchange with land biota, Nature, 376, 240–243, 1995. 19053

Dong, X., Xi, B., Kennedy, A., Feng, Z., Entin, J. K., Houser, P. R., Schiffer, R. A., L'Ecuyer, T., Olson, W. S., Hsu, K.-l., Liu, W. T., Lin, B., Deng, Y., and Jiang, T.: Investigation of the 2006 drought and 2007 flood extremes at the Southern Great Plains through an integrative analysis of observations, J. Geophys. Res.-Atmos., 116, D03204, doi:10.1029/2010JD014776, 2011. 19067

Ferraioli, L., Hueller, M., Vitale, S., Heinzel, G., Hewitson, M., Monsky, A., and Nofrarias, M.: Calibrating spectral estimation for the LISA Technology Package with multichannel syn-

ACPD
13, 19051–19083, 2013

thetic noise generation, Phys. Rev. D, 82, 042001, doi:10.1103/PhysRevD.82.042001, 2010. 19058, 19059

Gourdji, S. M., Mueller, K. L., Yadav, V., Huntzinger, D. N., Andrews, A. E., Trudeau, M., Petron, G., Nehrkorn, T., Eluszkiewicz, J., Henderson, J., Wen, D., Lin, J., Fischer, M., Sweeney, C., and Michalak, A. M.: North American CO_2 exchange: inter-comparison of modeled estimates with results from a fine-scale atmospheric inversion, Biogeosciences, 9, 457–475, doi:10.5194/bg-9-457-2012, 2012. 19053

Heffter, J. L.: Transport layer depth calculations, in: Second Joint Conference on Applications of Air Pollution Meteorology, American Meteorological Society, New Orleans, LA, 1980. 19059

Helliker, B. R., Berry, J. A., Betts, A. K., Bakwin, P. S., Davis, K. J., Denning, A. S., Ehleringer, J. R., Miller, J. B., Butler, M. P., and Ricciuto, D. M.: Estimates of net CO_2 flux by application of equilibrium boundary layer concepts to CO_2 and water vapor measurements from a tall tower, J. Geophys. Res.-Atmos., 109, D20106, doi:10.1029/2004JD004532, 2004. 19053

Hurwitz, M. D., Ricciuto, D. M., Bakwin, P. S., Davis, K. J., Wang, W. G., Yi, C. X., and Butler, M. P.: Transport of carbon dioxide in the presence of storm systems over a Northern Wisconsin forest, J. Atmos. Sci., 61, 607–618, 2004. 19054

Jenkins, G. M. and Watts, D. G.: Spectral Analysis and its Applications, Holden-Day, Oakland, California, 1969. 19057

Krol, M., Houweling, S., Bregman, B., van den Broek, M., Segers, A., van Velthoven, P., Peters, W., Dentener, F., and Bergamaschi, P.: The two-way nested global chemistry-transport zoom model TM5: algorithm and applications, Atmos. Chem. Phys., 5, 417–432, doi:10.5194/acp-5-417-2005, 2005. 19060

Lai, C.-T., Schauer, A. J., Owensby, C., Ham, J. M., Helliker, B., Tans, P. P., and Ehleringer, J. R.: Regional CO_2 fluxes inferred from mixing ratio measurements: Estimates from flask air samples in central Kansas, USA, Tellus B, 58, 523–536, 2006. 19053

Lawrence, M. G. and Salzmann, M.: On interpreting studies of tracer transport by deep cumulus convection and its effects on atmospheric chemistry, Atmos. Chem. Phys., 8, 6037–6050, doi:10.5194/acp-8-6037-2008, 2008. 19065

Lin, J. C., Gerbig, C., Wofsy, S. C., Daube, B. C., Matross, D. M., Chow, V. Y., Gottlieb, E., Andrews, A. E., Pathmathevan, M., and Munger, J. W.: What have we learned from intensive atmospheric sampling field programmes of CO_2?, Tellus B, 58, 331–343, 2006. 19054

ACPD
13, 19051–19083, 2013

Liu, J., Fung, I., Kalnay, E., and Kang, J.-S.: CO_2 transport uncertainties from the uncertainties in meteorological fields, Geophys. Res. Lett., 38, L12808, doi:10.1029/2011GL047213, 2011. 19053, 19067

Mesinger, F., DiMego, G., Kalnay, E., Mitchell, K., Shafran, P. C., Ebisuzaki, W., Jovic, D., Woollen, J., Rogers, E., Berbery, E. H., Ek, M. B., Fan, Y., Grumbine, R., Higgins, W., Li, H., Lin, Y., Manikin, G., Parrish, D., and Shi, W.: North American regional reanalysis, B. Am. Meteorol. Soc., 87, 343–360, doi:10.1175/BAMS-87-3-343, 2006. 19059

Parazoo, N. C., Denning, A. S., Berry, J. A., Wolf, A., Randall, D. A., Kawa, S. R., Pauluis, O., and Doney, S. C.: Moist synoptic transport of CO_2 along the mid-latitude storm track, Geophys. Res. Lett., 38, L09804, doi:10.1029/2011GL047238, 2011. 19054

Patra, P. K., Law, R. M., Peters, W., Roedenbeck, C., Takigawa, M., Aulagnier, C., Baker, I., Bergmann, D. J., Bousquet, P., Brandt, J., Bruhwiler, L., Cameron-Smith, P. J., Christensen, J. H., Delage, F., Denning, A. S., Fan, S., Geels, C., Houweling, S., Imasu, R., Karstens, U., Kawa, S. R., Kleist, J., Krol, M. C., Lin, S. J., Lokupitiya, R., Maki, T., Maksyutov, S., Niwa, Y., Onishi, R., Parazoo, N., Pieterse, G., Rivier, L., Satoh, M., Serrar, S., Taguchi, S., Vautard, R., Vermeulen, A. T., and Zhu, Z.: TransCom model simulations of hourly atmospheric CO_2: Analysis of synoptic-scale variations for the period 2002–2003, Global Biogeochem. Cy., 22, GB4013, doi:10.1029/2007GB003081, 2008. 19053

Peters, W., Jacobson, A. R., Sweeney, C., Andrews, A. E., Conway, T. J., Masarie, K., Miller, J. B., Bruhwiler, L. M. P., Petron, G., Hirsch, A. I., Worthy, D. E. J., van der Werf, G. R., Randerson, J. T., Wennberg, P. O., Krol, M. C., and Tans, P. P.: An atmospheric perspective on North American carbon dioxide exchange: CarbonTracker, P. Natl. Acad. Sci. USA, 104, 18925–18930, 2007. 19061

Potter, C. S., Randerson, J. T., Field, C. B., Matson, P. A., Vitousek, P. M., Mooney, H. A., and Klooster, S. A.: Terrestrial ecosystem production – a process model based on global satellite and surface data, Global Biogeochem. Cy., 7, 811–841, 1993. 19060

Randerson, J. T., Thompson, M. V., Conway, T. J., Fung, I. Y., and Field, C. B.: The contribution of terrestrial sources and sinks to trends in the seasonal cycle of atmospheric carbon dioxide, Global Biogeochem. Cy., 11, 535–560, 1997. 19060

Stephens, B. B., Gurney, K. R., Tans, P. P., Sweeney, C., Peters, W., Bruhwiler, L., Ciais, P., Ramonet, M., Bousquet, P., Nakazawa, T., Aoki, S., Machida, T., Inoue, G., Vinnichenko, N., Lloyd, J., Jordan, A., Heimann, M., Shibistova, O., Langenfelds, R. L., Steele, L. P.,

ACPD
13, 19051–19083, 2013

Francey, R. J., and Denning, A. S.: Weak northern and strong tropical land carbon uptake from vertical profiles of atmospheric CO_2, Science, 316, 1732–1735, 2007. 19066
Stull, R. B.: An Introduction to Boundary Layer Meteorology, Kluwer Academic Publishers, Dordrecht, the Netherlands, 1988. 19065
Styles, J. M., Lloyd, J., Zolotoukhine, D., Lawton, K. A., Tchebakova, N., Francey, R. J., Arneth, A., Salamakho, D., Kolle, O., and Schulze, E. D.: Estimates of regional surface carbon dioxide exchange and carbon and oxygen isotope discrimination during photosynthesis from concentration profiles in the atmospheric boundary layer, Tellus B, 54, 768–783, 2002. 19055
Vallis, G. K., Gerber, E. P., Kushner, P. J., and Cash, B. A.: A mechanism and simple dynamical model of the North Atlantic Oscillation and annular modes, J. Atmos. Sci., 61, 264–280, 2004. 19062
Viterbo, P. and Beljaars, A. C. M.: An improved land-surface parameterization scheme in the ECMWF model and its validation, J. Climate, 8, 2716–2748, 1995. 19061
von Storch, H. and Zwiers, F. W.: Statistical Analysis in Climate Research, Cambridge University Press, Cambridge, United Kingdom, 2004. 19061
Webb, E. K., Pearman, G. I., and Leuning, R.: Correction of flux measurements for density effects due to heat and water-vapor transfer, Q. J. Roy. Meteor. Soc., 106, 85–100, 1980. 19059
Williams, I. N., Riley, W. J., Torn, M. S., Berry, J. A., and Biraud, S. C.: Using boundary layer equilibrium to reduce uncertainties in transport models and CO_2 flux inversions, Atmos. Chem. Phys., 11, 9631–9641, doi:10.5194/acp-11-9631-2011, 2011. 19053, 19055
Yi, C., Davis, K. J., Bakwin, P. S., Denning, A. S., Zhang, N., Desai, A., Lin, J. C., and Gerbig, C.: Observed covariance between ecosystem carbon exchange and atmospheric boundary layer dynamics at a site in northern Wisconsin, J. Geophys. Res.-Atmos., 109, D08302, doi:10.1029/2003JD004164, 2004. 19053

ACPD
13, 19051–19083, 2013

Table 1. Summer (JJA) biases in inverse surface CO_2 flux estimates for two prior flux uncertainties (P_1 and P_2) with imposed 0.2 ppm bias in simulated vertical gradients. The P_1 case is tightly constrained to the concentration measurements, whereas the P_2 case is tightly constrained to the perfectly specified prior flux. Prior flux uncertainties are scaled according to σ, the standard deviation of F.

Prior Flux Uncertainty	Bias	
	F [μmol m^{-2} s^{-1}]	ΔC [ppm]
$P_1 = \sigma$	−0.15 (−13 %)	0.01 (0.4 %)
$P_2 = 0.01\sigma$	< 0.01 (0.3 %)	0.21 (7.4 %)

ACPD
13, 19051–19083, 2013

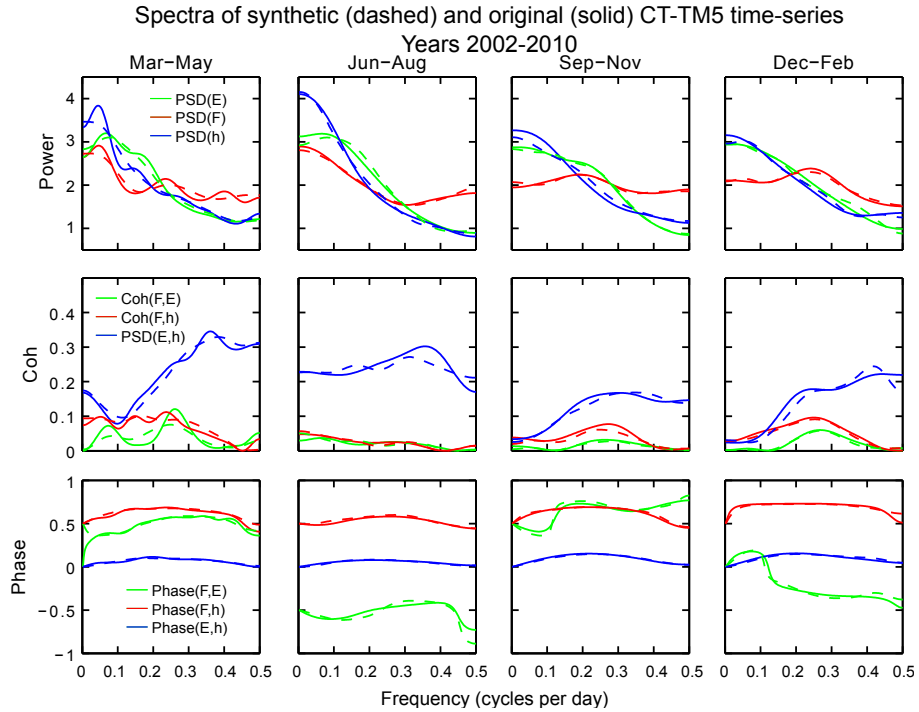

Fig. 1. Top row: Power spectral density estimates for entrainment (E, green lines), surface and horizontal CO_2 flux (F, red lines), and boundary layer height (h, blue lines), for original CT-TM5 time-series (solid) and synthetic CT-TM5 time-series (dashed) for each season, normalized to have equal area under each curve (equal standard deviation). Middle row: Coherence spectra corresponding to the cross spectral densities $CSD_{F,E}$ (green), $CSD_{F,h}$ (red), and $CSD_{E,h}$ (blue). Bottom row: Phase spectra corresponding to the cross spectral densities $CSD_{F,E}$ (green), $CSD_{F,h}$ (red), and $CSD_{E,h}$ (blue).

ACPD
13, 19051–19083, 2013

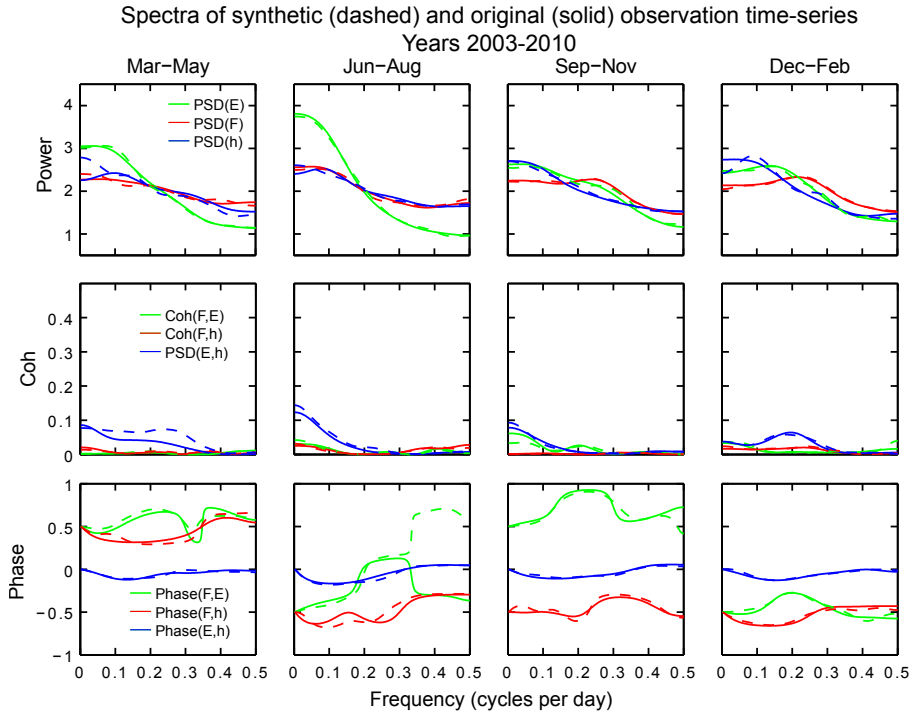

Fig. 2. Top row: Power spectral density estimates for entrainment (E, green lines), surface and horizontal CO_2 flux (F, red lines), and boundary layer height (h, blue lines), for original observational time-series (solid) and synthetic observational time-series (dashed) for each season, normalized to have equal area under each curve. Middle row: Coherence spectra corresponding to the cross spectral densities $CSD_{F,E}$ (green), $CSD_{F,h}$ (red), and $CSD_{E,h}$ (blue). Bottom row: Phase spectra corresponding to the cross spectral densities $CSD_{F,E}$ (green), $CSD_{F,h}$ (red), and $CSD_{E,h}$ (blue).

ACPD
13, 19051–19083, 2013

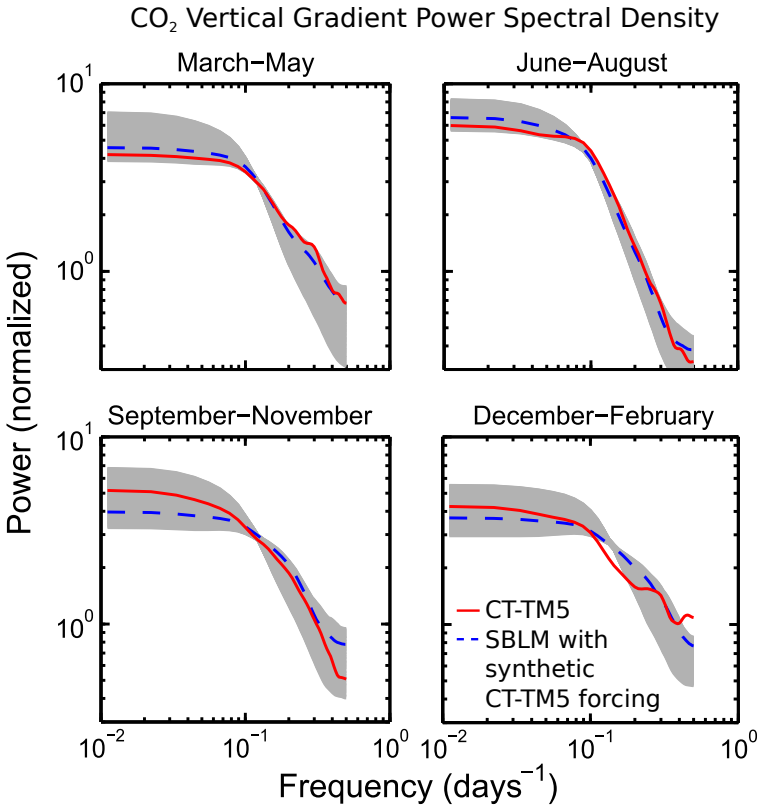

Fig. 3. Normalized power spectral densities for boundary layer CO_2 concentrations predicted by the stochastic boundary layer model (SBLM) with synthetic CT-TM5 forcing (dashed blue), and spectral densities for the original boundary layer CO_2 concentrations from the CT-TM5 data assimilation system (red). The gray shading indicates the range of SBLM solutions for $0 < f < 1.25$, where f is an estimated sub-grid scale boundary layer entrainment expressed as a fraction of the resolved-scale vertical velocity (see text for details).

ACPD
13, 19051–19083, 2013

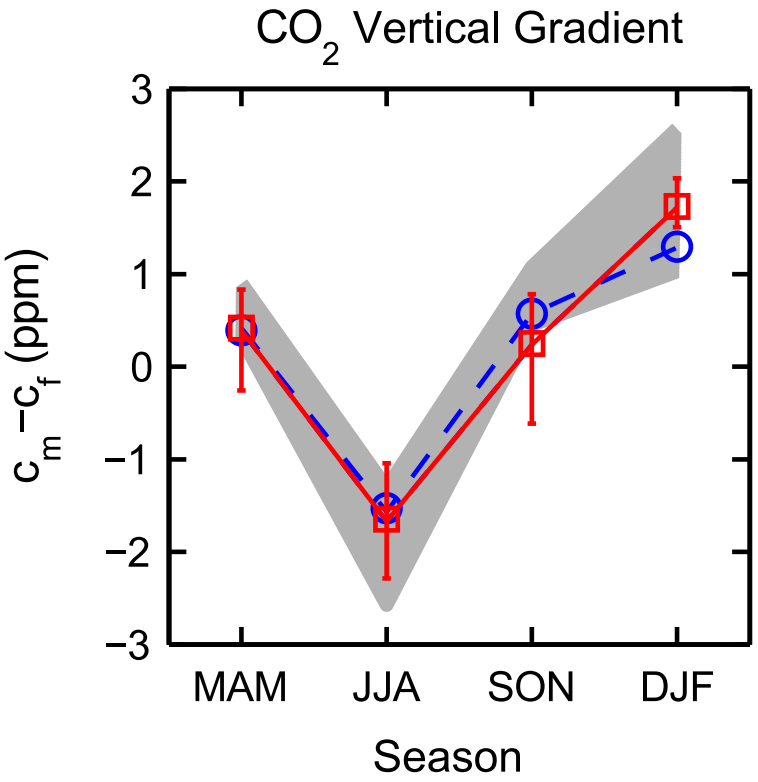

Fig. 4. Seasonally-averaged vertical CO_2 gradients ($c_m - c_f$) predicted by SBLM with synthetic CT-TM5 forcing (dashed blue, corresponding to dashed blue lines in Fig. 3); and the original vertical CO_2 gradient from the CT-TM5 data assimilation system (red). Gray shading indicates the range of solutions for a range of sub-grid scale boundary layer entrainment (as in Fig. 3); gradients monotonically decrease in magnitude with stronger entrainment. Error bars indicate the maxima and minima of seasonally-averaged gradients for the 8 yr period.

ACPD
13, 19051–19083, 2013

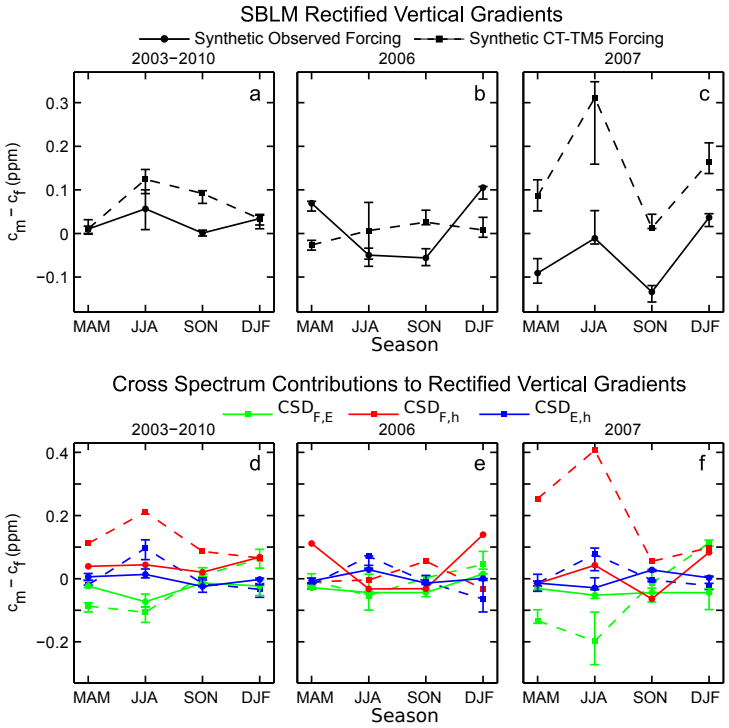

Fig. 5. (a–c) Rectified vertical CO_2 gradients ($c_m - c_f$) predicted by SBLM forced with synthetic observations (solid) and synthetic CT-TM5 (dashed) having multivariate cross spectra fitted to the original time-series, as shown in Figs. 1, 2. The stochastic model was fitted to cross spectra estimated over years 2002–2010 **(a)**, and for years 2006 **(b)** and 2007 **(c)**. **(d–f)** show separate contributions to the rectified gradients by each bivariate cross spectrum: $CSD_{F,E}$ (green), $CSD_{F,h}$ (red), and $CSD_{E,H}$ (blue). Rectified gradients are defined relative to a control vertical gradient given by the solution to SBLM forced with synthetic time-series having all zero cross spectra. Error bars show the range of solutions for 25 % weaker and 25 % stronger sub-grid scale entrainment (see text for details).

ACPD
13, 19051–19083, 2013

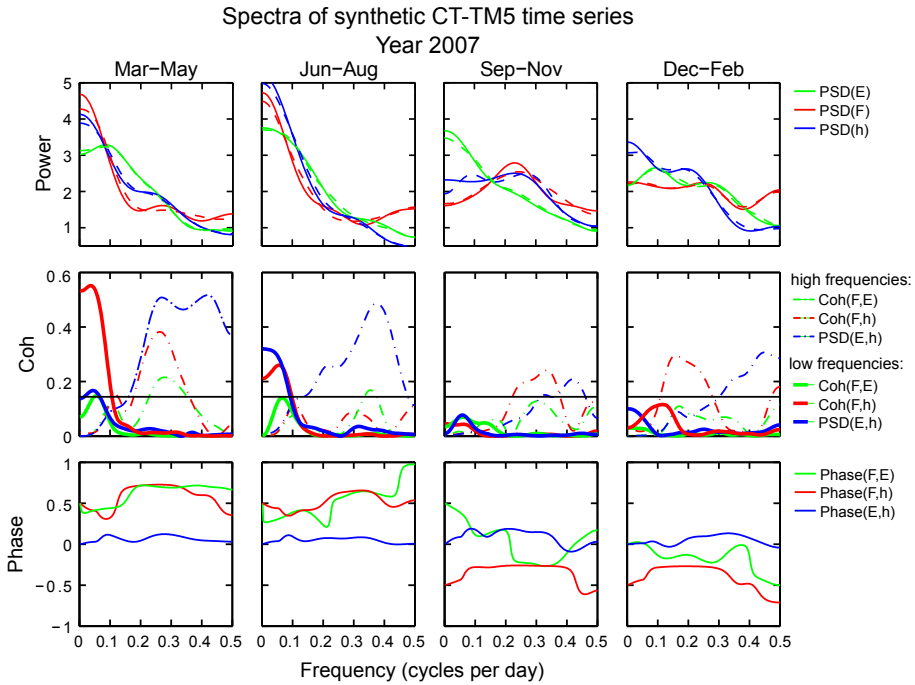

Fig. 6. Top row: Power spectral densities of E (green), F (red), and h (blue), estimated from CT-TM5 forcing time-series for year 2007, normalized to have equal area under each curve. Middle row: Coherence spectra corresponding to the cross spectral densities $CSD_{F,E}$ (green), $CSD_{F,h}$ (red), and $CSD_{E,h}$ (blue), separated into contributions from low-frequencies (thick lines) and high-frequencies (dot-dashed lines), with a separation time-scale of 10-days (0.1 cycles per day). Bottom row: Phase spectra corresponding to the cross spectral densities $CSD_{F,E}$ (green), $CSD_{F,h}$ (red), and $CSD_{E,h}$ (blue). The horizontal black line (middle row) indicates the 90 % confidence level for coherence.

ACPD
13, 19051–19083, 2013

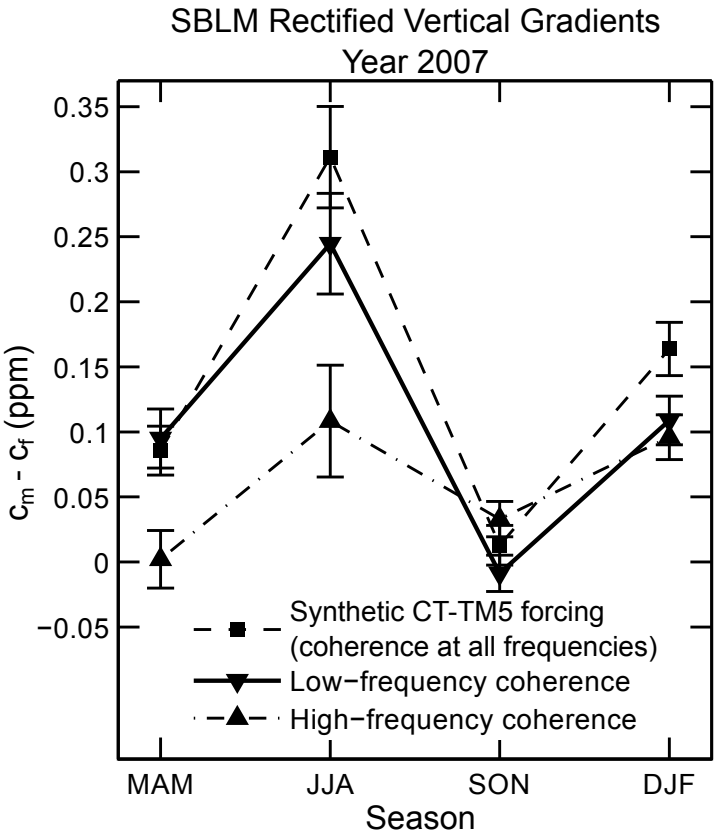

Fig. 7. Rectified vertical CO_2 gradients predicted by SBLM with synthetic forcing fitted to modified cross-spectral densities having the coherence spectra shown in Fig. 6. The modified forcing time-series have coherence spectra separated into low-frequencies (downward triangles) or high-frequencies (upward triangles). The unmodified forcing time-series is shown for reference (dashed line, solid squares), and corresponds to the dashed line in Fig. 5c. Error bars indicate the standard error of the mean over 300 independent realizations of each season.

ACPD
13, 19051–19083, 2013